PAPER

Check for updates

Photoexcited charge manipulation in conjugated polymers bearing a Ru(ii) complex catalyst for visible-light CO$_2$ reduction†

Akinobu Nakada, [ID] *[ab] Ryuichi Miyakawa,[a] Ren Itagaki,[a] Kosaku Kato, [ID] [c] Chinami Takashima,[d] Akinori Saeki, [ID] [e] Akira Yamakata, [ID] [c] Ryu Abe, [ID] [f] Hiromi Nakai [ID] [dgh] and Ho-Chol Chang [ID] *[a]

Conjugated polymers have emerged as promising candidates for photocatalyst materials. Design principles that maximize the synergy between the conjugated skeleton and catalyst moiety are strongly desired to be established for achieving efficient photocatalysis. Herein, the photoexcited charge manipulation was demonstrated by molecular engineering in conjugated polymers bearing a Ru(ii) complex as the CO$_2$ reduction photocatalyst. Combinational studies based on ultrafast spectroscopies and theoretical calculations revealed that the introduction of an electron-donating carbazole (Cz) skeleton in the polymer enables enhanced photoexcited charge trapping on the Ru(ii)-complex catalyst moiety. The carbazole-based polymer **[Cz-bpyRu]**$_n$ facilitates CO$_2$ reduction under visible light even longer than 500 nm and exhibited 7- to 15-fold greater activity than those of phenyl (Ph) and benzothiadiazole (Bt) counterparts. The findings of this study thus provide insights into molecular engineering for photoexcited charge manipulation to achieve efficient photocatalysis.

Akinobu Nakada is a Senior Lecturer at Kyoto University. He received his PhD from Tokyo Institute of Technology in 2017. During 2017–2018, he joined Kyoto University as a Post-doctoral Fellow and a specially-appointed Assistant Professor. After serving as an Assistant Professor at Chuo University from 2019 to 2021, he was promoted to the present position at Kyoto University in 2022. From 2020, he concurrently serves as a PRESTO researcher of Japan Science and Technology Agency. His research interests include molecular engineering into photocatalyst materials/systems for light-to-chemical conversion.

Introduction

Reductive conversion of CO$_2$ into energy-added molecules has been an important subject in various fields including materials chemistry,[1,2] catalysis,[3,4] electrochemistry,[5,6] and photochemistry,[7,8] from viewpoints of both decreasing CO$_2$ concentration and gaining energy and carbon resources.[9–11] In particular, the development of photocatalyst materials, which facilitate CO$_2$ reduction without high temperature and/or pressure, has been regarded as a promising way.[7,8]

For the past four decades, molecular-based photocatalysts including metal complexes[12,13] and semiconductor-based photocatalysts including metal oxides[14–16] and mixed-anion materials[16,17] have been extensively studied. High selectivity for CO$_2$ reduction, based on well-defined and tunable active sites, is one of the advantages of molecular photocatalysts, as has been demonstrated so far.[12,18] Another important priority of

[a]*Department of Applied Chemistry, Faculty of Science and Engineering, Chuo University, 1-13-27 Kasuga, Bunkyo-ku, Tokyo 112-8551, Japan. E-mail: nakada@scl.kyoto-u.ac.jp; chang@kc.chuo-u.ac.jp*

[b]*Precursory Research for Embryonic Science and Technology (PRESTO), Japan Science and Technology Agency (JST), 4-1-8 Honcho, Kawaguchi, Saitama 332-0012, Japan*

[c]*Graduate School of Engineering, Toyota Technological Institute, 2-12-1 Hisakata, Tempaku-ku, Nagoya 468-8511, Japan*

[d]*Waseda Research Institute for Science and Engineering (WISE), Department of Chemistry and Biochemistry, School of Advanced Science and Engineering, Waseda University, 3-4-1 Okubo, Shinjuku, Tokyo 169-8555, Japan*

[e]*Department of Applied Chemistry, Graduate School of Engineering, Osaka University, 2-1 Yamadaoka, Suita, Osaka 565-0871, Japan*

[f]*Department of Graduate School of Engineering, Kyoto University, Katsura, Nishikyo-ku, Kyoto 615-8510, Japan*

[g]*Waseda Research Institute for Science, Waseda University, 3-4-1 Okubo, Shinjuku, Tokyo 169-8555, Japan*

[h]*Elements Strategy Initiative for Catalysts & Batteries (ESICB), Kyoto University, 1-30 Goryo-Ohara, Nishikyo-ku, Kyoto 615-8245, Japan*

† Electronic supplementary information (ESI) available. See https://doi.org/10.1039/d2ta02183h

This journal is © The Royal Society of Chemistry 2022

J. Mater. Chem. A, 2022, **10**, 19821–19828 | 19821

molecular photocatalysis is the designability of molecular orbitals in order to facilitate transfer and separation of photo-excited charges for the efficient photocatalysis even under visible-light illumination.[13]

On the other hand, semiconductor photocatalysts have advantageous in terms of band formation.[8,15] The band-gap excitation of semiconductors generates multiple electrons and holes in the conduction and valence bands. Therefore, simultaneous multi-electron reduction and oxidation reactions, *e.g.*, overall water splitting[19–22] and CO_2 reduction using water as the electron source,[16] have been accomplished using a number of semiconductor photocatalysts, while such reactions have hardly been reported using a molecular photocatalyst system.[23] In terms of CO_2 reduction, however, semiconductor photocatalysts frequently suffer from the low selectivity of CO_2 reduction by competing with efficient proton reduction.[16] Recently, molecular-semiconductor hybrid photocatalysts have been developed to maximize their advantages, although it still remains a challenge for efficient photocatalytic CO_2 reduction.[24–26]

Recently, organic conjugated polymers have emerged as new candidates for photocatalyst materials.[27,28] The organic polymers not only exhibit semiconducting properties due to the extended π-conjugation but also have the molecular designability.[29] To date, organic polymer-based photocatalysts have been developed for CO_2 reduction under visible light.[30–39] Metal-based catalytic sites[31,33–35,39] are frequently required to selectively reduce CO_2 although some organic polymers are reported to facilitate metal-free CO_2 reduction.[30,32,36–38] Hence, the design principle, that maximizes the synergy between the conjugated skeleton and catalyst moiety, is strongly desired for achieving efficient photocatalytic CO_2 reduction. Several combinations of the metal-based catalytic sites and organic polymers have been developed so far,[31,33–35,39] while the design principles, particularly to manipulate the excited charge carrier have not been established satisfactorily. Herein, we show strong impacts of excited charge distribution in conjugated polymer photocatalysts with a site-selectively incorporated Ru(II) complex catalyst (Fig. 1a), which are elucidated by a combination of ultrafast spectroscopy and theoretical calculation, on their photocatalytic activity for CO_2 reduction.

Results and discussion

[X-bpy]$_n$ (X = Ph, Bt, and Cz) were synthesized by the Suzuki–Miyaura cross-coupling reaction between 5,5′-dibromo-2,2′-bipyridine (Br_2bpy) and diboronic acids or esters corresponding to the X moieties (X-(B(OR)$_2$)$_2$) with the aid of the Pd(PPh$_3$)$_4$ catalyst (Fig. 1a). MALDI-TOF-MS spectra of the obtained materials gave repeated peaks with interpeak *m/z* differences corresponding to the **X-bpy** unit (Fig. S1†), indicative of the formation of –[**X-bpy**]– conjugated networks. The maximum numbers of connected units detected in the MALDI-TOF-MS spectra were 16, 32, and 19 for [Cz-bpy]$_n$, [Ph-bpy]$_n$, and [Bt-bpy]$_n$, respectively. ATR-FT-IR spectra of [X-bpy]$_n$, which exhibited specific peaks similar to the model monomers
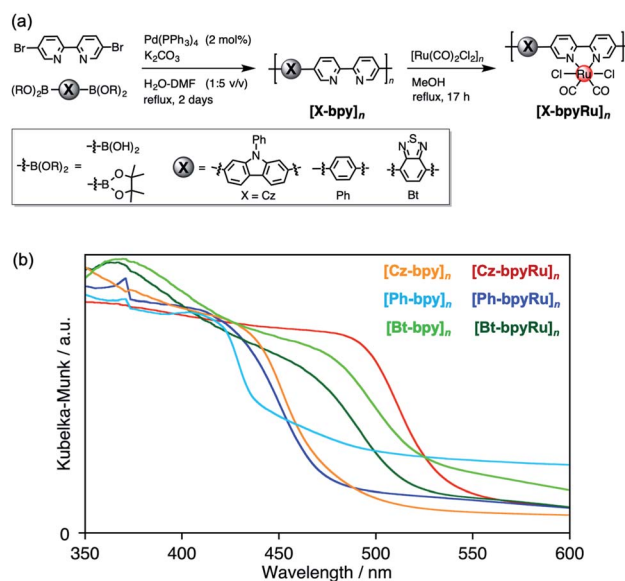

Fig. 1 (a) Synthetic procedures and (b) UV-vis diffuse reflectance spectra of the polymer photocatalysts developed in this study.

corresponding to the X and bpy units, supported that the X and bpy skeletons were maintained (Fig. S2–S4†).

A Ru(II)-complex catalyst moiety was introduced by refluxing [Ru(CO)$_2$Cl$_2$]$_n$ and the polymers [X-bpy]$_n$ in methanol. The obtained powder exhibited characteristic CO vibrations at 2054 and 1990 cm^{-1} assignable to the Ru(bpy)(CO)$_2$Cl$_2$-type coordination environment regardless of the type of X, indicative of successful post-complexation of the Ru(CO)$_2$Cl$_2$ unit to the bipyridine moiety in [X-bpy]$_n$ as the ligand (Fig. S2–S4†). Based on elemental analyses, the introduced Ru complex moieties were estimated to be at least *ca.* 2/3 of the bpy skeleton for all [X-bpyRu]$_n$. The Ru(II) complex-incorporated polymers are denoted as [X-bpyRu]$_n$. Scanning electron microscope (SEM) images and XRD patterns suggested that the obtained materials had indefinite low-crystalline structures (Fig. S5 and S6†). We also tried to directly synthesize [Cz-bpyRu]$_n$ by Suzuki–Miyaura cross-coupling between Cz-(B(OR)$_2$)$_2$ and the as-synthesized Ru(Br$_2$bpy)(CO)$_2$Cl$_2$. However, the CO vibration peaks in IR spectra were shifted to 2019 and 1923 cm^{-1} after the reaction (Fig. S7†), suggesting that the Ru(bpy)(CO)$_2$Cl$_2$-type coordination environment was not maintained, but there was a formation of a [Ru(bpy)(CO)$_2$]$_n$-type network with Ru–Ru bonds.[40,41] Therefore, we concluded that the post complexation method is more suitable for the precise synthesis of the conjugated polymer with structurally well-defined Ru(II) complex catalyst, and will describe the post-complexation polymer unless otherwise noted.

In contrast to the colorless building-block monomers (Fig. S8†), the obtained polymers exhibited largely red-shifted absorption covering the visible region due to the formation of the extended π-conjugation (Fig. 1b), as reported for conventional conjugated polymers.[27,28] The band positions for each material, which were estimated by the bandgaps (E_g) and the ionization energies determined using photoelectron yield

spectroscopy (PYS),[42] are shown in Fig. 2. Focusing on the Ru non-incorporated materials, electron-deficient Bt (E_g = 2.25 eV) and electron-rich Cz (E_g = 2.56 eV) made impacts the narrowing bandgaps compared with [Ph-bpy]$_n$ (E_g = 2.69 eV).

To gain further insights into the roles of X moieties in the electron transition, we conducted a theoretical calculation of molecular orbitals for the model monomers X-bpy (Fig. 2). Regardless of the X moiety, the frontier orbitals were located around the π-conjugated skeletons. The π–π*-based HOMO–LUMO distribution shows, however, different nature depending on the X moiety. In the cases of Ph-bpy, both HOMO and LUMO are delocalized on the whole conjugated skeleton. In contrast, charge-transfer characters can be found in the HOMO–LUMO electron transition in the cases of X = Cz and Bt, but the roles of Cz and Bt are different. The electron-rich Cz in Cz-bpy appeared to be HOMO for donating an electron to the bpy unit, whereas electron-deficient Bt serves as an acceptor (i.e., LUMO in Bt-bpy). The character of donor–acceptor charge transfer should decrease the E_g values of [Cz-bpy]$_n$ and [Bt-bpy]$_n$, in which the electron-donating Cz increases the HOMO energy while the electron-withdrawing Bt decreases the LUMO energy, respectively.

Notably, the introduction of the Ru(II) complex unit further modified the HOMO–LUMO potentials of the polymers. In the case of X = Ph, LUMO energies decreased with a slightly decreased bandgap (ca. 0.1 eV) after introducing the Ru(II) complex. Since LUMO are delocalized over the whole π-conjugated system in Ph-bpy and Ph-bpyRu (Fig. 2), these potential shifts can be understood by stabilization of the π-conjugated system through coordination of the bpy moiety to the Ru(II) center.[43] At a glance, the X = Cz system exhibits a similar trend to that of X = Ph, whereas a larger degree of bandgap narrowing from [Cz-bpy]$_n$ (E_g = 2.6 eV) to [Cz-bpyRu]$_n$ (E_g = 2.3 eV) was obviously observed as a specific feature of the X = Cz system

(Fig. 2). The HOMO and LUMO of Cz-bpyRu separately distribute at the Cz and bpy moieties, respectively. Therefore, LUMO localized on bpy was selectively stabilized by the coordination to the Ru(II) center, leading to a decreased bandgap in the case of [Cz-bpyRu]$_n$. Interestingly, introducing the Ru(II) complex to [Bt-bpy]$_n$ increased both HOMO–LUMO energies with a slightly expanded bandgap (Fig. 2). The Ru d orbitals participated in the formation of HOMO of Bt-bpyRu, in contrast to the X = Cz system in which both HOMO–LUMO are constructed by the organic conjugated chain without the direct contribution of Ru d orbitals. The different origins of HOMO between Bt-bpy (π orbitals) and Bt-bpyRu (Ru d orbitals) might elevate the HOMO level by introducing the Ru(II) complex moiety, although the reason for the destabilization of LUMO by introducing the Ru(II) complex moiety is unclear at this stage. From these results, we can conclude that the opposite trends in the HOMO–LUMO shifts, when introducing the Ru(II) complex moiety, are caused by the electron-donating or withdrawing nature of unit X. The photoexcited charge distribution for X-bpyRu was evaluated by the differential Mulliken population between the ground and excited states. The differential charges on the bpyRu moiety were −0.057, 0.001, and 0.021 for Cz-bpyRu, Ph-bpyRu, and Bt-bpyRu, respectively (Table S1†). These results suggest that Cz-bpyRu generates photoexcited electrons relatively located on the bpyRu moiety, while Bt-bpyRu generates it on the opposite side. As mentioned in the Introduction, not only the HOMO–LUMO gap but also its potential and spatial distribution are important to manipulate photoexcited charge carriers to be effectively utilized at the catalytic moiety. Thus, the direct or indirect cooperation of π-the conjugated system and metal d-orbitals will expand the tunability of HOMO–LUMO level, gap, and distribution for the development of suitable photocatalyst materials.

Fig. 2 Experimentally-estimated band positions of [X-bpyM]$_n$ (X = Cz, Ph, and Bt; M = none and Ru) along with calculated HOMO (lower) and LUMO (upper) distributions of X-bpyM.

This journal is © The Royal Society of Chemistry 2022

J. Mater. Chem. A, 2022, 10, 19821–19828 | 19823

Prior to photocatalysis studies, behaviors of photoexcited carriers in the polymer materials were evaluated by means of transient spectroscopy. Fig. 3 shows transient photoconductivity signals of $[\text{X-bpyM}]_n$, which were obtained using time-resolved microwave conductivity (TRMC) measurements upon laser excitation ($\lambda = 355$ nm). The photoconductivity values $\phi\Sigma\mu$, where ϕ, the quantum efficiency of charge carrier generation and $\Sigma\mu$, the sum of photogenerated carrier mobilities, are increased within the instrumental time resolution ($\sim 10^{-7}$ s) and then gradually decreased due to charge recombination and/or trapping. The maximum photoconductivity values $\phi\Sigma\mu_{\text{max}}$[44] were similar among three $[\text{X-bpy}]_n$ compounds (compare grey bars in Fig. 3d). The incorporation of the Ru(II) complex moiety into the bpy ligand led to the decreased $\phi\Sigma\mu_{\text{max}}$ in the case of X = Cz (Fig. 3a and d). Since the main structures of the polymers are maintained by post complexation of the $\text{Ru(CO)}_2\text{Cl}_2$ unit (Fig. S2–S4†), the decreased photoconductivity of $[\text{Cz-bpyRu}]_n$ compared with $[\text{Cz-bpy}]_n$ is likely due to the charge trapping at the Ru(II) complex moiety. A similar phenomenon was observed in the case of X = Ph although the degree was smaller than that of X = Cz (Fig. 3b and d). In contrast, the $[\text{Bt-bpyM}]_n$ system showed negligible change trapping by incorporating the Ru complex moiety (Fig. 3c and d).

For an in-depth understanding of the origin of photoexcited charge trapping, time-resolved infrared (TR-IR) absorption measurements were performed. We focused on the characteristic absorption corresponding to the CO vibration in the $\text{Ru(bpy)(CO)}_2\text{Cl}_2$ moiety, which reflects the changes in electronic densities at the Ru center.[45] Upon laser excitation ($\lambda = 420$ nm) to $[\text{Cz-bpyRu}]_n$, absorption bands at around 2069 and 2007 cm^{-1} decreased, whereas lower-energy bands at around 2045 and 1977 cm^{-1} increased within 1 ps (Fig. 4a). Such derivative-type differential spectra approximately centered at

Fig. 4 Ground state FT-IR (upper) and TR-IR (lower) spectra of (a) $[\text{Cz-bpyRu}]_n$, (b) $[\text{Ph-bpyRu}]_n$, and (c) $[\text{Bt-bpyRu}]_n$, along with (d) time courses of the differential absorbance at 2045 cm^{-1} and 2069 cm^{-1} (red: $[\text{Cz-bpyRu}]_n$, blue: $[\text{Ph-bpyRu}]_n$, and green: $[\text{Bt-bpyRu}]_n$).

absorption peaks of the ground state (2060 and 1994 cm^{-1}) are characteristic of the simultaneous decay and rise of the ground state and a new state, respectively.[46] Kubiak et al. reported that one-electron reduction of $\text{Ru(bpyR}_2)(\text{CO})_2\text{Cl}_2$ (bpyR$_2$ = 6,6'-dimethythyl-2,2'-bipyridine) induces lower-energy shifts of CO vibration with 25–30 cm^{-1} owing to the enhanced back donation from the electron-rich Ru center.[45] Hence, it is strongly suggested that the photoexcitation of $[\text{Cz-bpyRu}]_n$ generates a reduced Ru complex moiety through the excited charge trapping. Although $[\text{Ph-bpyRu}]_n$ and $[\text{Bt-bpyRu}]_n$ showed similar spectroscopic changes (Fig. 4b and c), $[\text{Cz-bpyRu}]_n$ exhibited the largest generation of the reduced catalyst moiety (Fig. 4d). The trends are in good agreement with those observed in TRMC (vide supra, Fig. 3). From the aforementioned transient spectroscopy, we can conclude that photoexcited electrons are captured at the Ru(II) complex moiety more effectively in $[\text{Cz-bpyRu}]_n$ compared with the X = Ph and Bt counterparts, in association with their LUMO distribution at the Ru(II) complex moiety (see Fig. 2).

Photocatalytic CO_2 reduction activities of the polymers were evaluated in a MeCN-TEOA (4 : 1 v/v) dispersion upon visible-light ($\lambda > 400$ nm) irradiation (Table 1). $[\text{Cz-bpyRu}]_n$ generated formate as the main product together with H_2 and a small amount of CO (Fig. 5a and entry 1 in Table 1). In the absence of photoirradiation, CO_2, or TEOA, almost no activity was found (entries 2–4, Table 1), indicating that this reaction represents a photochemical reduction of CO_2 using TEOA as an electron donor. By using $[\text{Cz-bpy}]_n$ instead of $[\text{Cz-bpyRu}]_n$, CO_2 reduction products became negligible and the main product switched to H_2 (entry 5 in Table 1). Therefore, it is strongly suggested that the Ru(II) complex moiety acts as the catalyst for CO_2 reduction. After 12 h photoirradiation, the photocatalysis deactivated (Fig. 5a). In ATR-FT-IR spectra, characteristic CO vibrations

Fig. 3 Transient conductivities of (a) $[\text{Cz-bpyM}]_n$, (b) $[\text{Ph-bpyM}]_n$, and (c) $[\text{Bt-bpyM}]_n$ (M = none (grey) or Ru (red)), along with (d) their maximum values ($\phi\Sigma\mu_{\text{max}}$) obtained by photoexcitation at $\lambda = 355$ nm.

19824 | J. Mater. Chem. A, 2022, 10, 19821–19828

This journal is © The Royal Society of Chemistry 2022

Table 1 Results of photocatalytic reactions using polymer photocatalysts[a]

Entry	Photocatalyst	Control	Product/μmol		
			Formate	CO	H_2
1	**[Cz-bpyRu]**$_n$	—[a]	24.7	0.8	7.8
2	**[Cz-bpyRu]**$_n$	Without light	N.D.	N.D.	N.D.
3	**[Cz-bpyRu]**$_n$	Without CO_2[b]	N.D.	Trace	N.D.
4	**[Cz-bpyRu]**$_n$	Without TEOA	N.D.	0.5	Trace
5	**[Cz-bpy]**$_n$	—[a]	0.5	N.D.	26.6
6	**[Ph-bpyRu]**$_n$	—[a]	3.6	0.4	0.5
7	**[Bt-bpyRu]**$_n$	—[a]	1.7	0.3	0.3

[a] 2 mg of photocatalyst powder in an MeCN-TEOA (2 mL; 4 : 1 v/v) dispersion was irradiated at $\lambda > 400$ nm for 12 h under CO_2 atmosphere. [b] Under N_2 atmosphere.
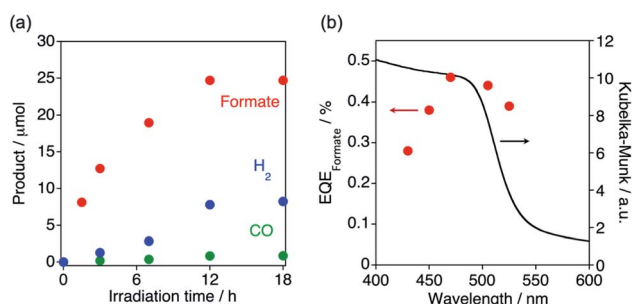

Fig. 5 (a) Time courses of photocatalytic reaction and (b) action spectra of external quantum efficiency of formate formation (EQE$_{formate}$) by **[Cz-bpyRu]**$_n$ (2 mg) in an MeCN-TEOA (2 mL; 4 : 1 v/v) dispersion under CO_2 atmosphere.

corresponding to Ru(bpy)(CO)$_2$Cl$_2$-type coordination environment were shifted to 2019 and 1923 cm^{-1} after photolysis, suggesting the formation of a [Ru(bpy)(CO)$_2$]$_n$-type network with Ru–Ru bonds (Fig. S9†). On the other hand, IR spectra corresponding to the organic skeleton were almost unchanged. Hence, we conclude that the changes in the Ru catalyst moiety have likely caused the deactivation. Although the stability leaves much room for improvement, the wavelength dependency of the formate formation clearly indicates that **[Cz-bpyRu]**$_n$ effectively utilizes its HOMO–LUMO photoexcitation even more than 500 nm for photocatalytic reaction (Fig. 5b). Maeda and co-workers reported that copolymerized organic polymers C$_3$N$_4$, which were modified with Ru(2,2′-bipyridine-4,4′-diphosphonic acid)(CO)$_2$Cl$_2$, facilitate the photocatalytic formate formation under $\lambda > 500$ nm visible light, while the quantum efficiency at $\lambda > 500$ nm was not reported.[47,48] The external quantum efficiencies for the formate formation (EQE$_{formate}$) by the present **[Cz-bpyRu]**$_n$ polymer were estimated to be 0.44% and 0.38% at 505 and 525 nm, respectively. These values are comparable to or better than that of a triazine-based conjugated polymer for CO formation,[30] which is one of the few examples of obtaining reliable quantum efficiency at $\lambda > 500$ nm visible light by using organic polymer-based photocatalysts.

Notably, **[Cz-bpyRu]**$_n$ exhibited 7- to 15-folds higher photocatalytic activity for CO_2 reduction than **[Ph-bpyRu]**$_n$ and **[Bt-**

bpyRu]$_n$ (compare entries 1, 6, and 7 in Table 1). Although the bulk structures possibly affect photocatalytic performance, all the **[X-bpyRu]**$_n$ polymers have similar indefinite low-crystalline bulk structures (*vide supra*, Fig. S5 and S6†). The different visible-light absorbability (Fig. 1a) might be a reason for their distinct photocatalytic activities. However, the trend of the formate-formation activity did not change even if a light centered at $\lambda = 430$ nm, where all **[X-bpyRu]**$_n$ can enough absorb, was irradiated (Fig. S10†). In addition, **[Cz-bpyRu]**$_n$ has a smaller driving force for both redox reactions than **[Ph-bpyRu]**$_n$ (Fig. 2). Therefore, the much better photocatalytic activity of **[Cz-bpyRu]**$_n$ most probably originated from its effective capturing of photogenerated electrons at the catalytic Ru(ɪɪ)-complex moiety, as demonstrated by means of transient spectroscopies (Fig. 3 and 4). From these results, we can conclude that precise HOMO–LUMO tuning *via* molecular engineering with an appropriate choice of the building block X in **[X-bpyRu]**$_n$ (Cz, Ph, or Bt) enables effective charge trapping at the structurally well-defined Ru(ɪɪ) complex catalyst unit, leading to the much efficient CO_2 photoreduction.

Conclusions

In this work, we constructed conjugated polymers bearing a Ru(ɪɪ) complex catalyst in the bipyridine-ligand moiety and unveiled the relationship between their molecular structures, HOMO–LUMO distributions, excited charge trapping, and photocatalytic activity for CO_2 reduction. The introduction of an electron-donating carbazole skeleton enables LUMO localization and effective trapping of the photoexcited electrons at the Ru(ɪɪ) catalyst moiety, engaging in 7- to 15-folds efficient CO_2 reduction compared with phenyl and benzothiadiazole counterparts. Hence, in this study, we demonstrate the effectiveness of the manipulation of local photoexcited charge distributions by the molecular engineering of organic polymers with a site-selectively incorporated molecular catalyst. The carbazole-based polymer **[Cz-bpyRu]**$_n$ utilizes visible light at more than 500 nm with a potential photocatalytic efficiency of CO_2 reduction, which is comparable to or better than that of the organic-polymer photocatalyst reported previously.[30] On the other hand, we should note that the activity of **[Cz-bpyRu]**$_n$ has still much room for improvement, possibly due to their indefinite low-crystalline bulk structure. Recently, research on crystal- and pore-structure engineering of organic-polymer photocatalysts including covalent organic frameworks have been accelerated so far.[28,33] Therefore, we believe that this strategy of manipulating photoexcited charge carriers expands the opportunity to develop efficient photocatalysts by coupling with well-established bulk engineering.

Experimental

General procedure

^{1}H NMR (400 MHz) spectra were measured on a JEOL ECZ-500R spectrometer. Elemental analyses were carried out on a Perkin-nElmer 2400 II CHN analyzer. UV-vis absorption and diffuse reflectance spectra were recorded at room temperature on

This journal is © The Royal Society of Chemistry 2022

J. Mater. Chem. A, 2022, **10**, 19821–19828 | **19825**

Shimadzu U1900i and U2600i spectrophotometers, respectively. Solid-state FT-IR spectra were measured on a Thermo-Fisher Nicolet 6700 spectrometer equipped with a Smart-Orbit (Diamond) attenuated total reflection (ATR) accessory. Solution FT-IR spectra were measured on a JASCO FT/IR-4100 spectrometer. MALDI-TOF-MS spectra were measured on a Shimadzu MALDI-8020 mass spectrometer. Scanning electron microscope (SEM) images were obtained using a Hitachi MC1000 at 10 kV after coating Pt on the samples. Powder X-ray diffraction patterns were recorded on a Rigaku Ultima IV diffractometer with Cu Kα radiation. Photoelectron yield spectra (PYS) were measured on a Bunko Keiki BIP-KV202GD apparatus. The PYS measurements provide the lowest ionization energies corresponding to the valence-band maximum potentials.[42,49]

Acetonitorile (MeCN; dehydrated, >99.5%), methanol (MeOH; dehydrated, >99.6%), CHCl$_3$ (>99.0%), CH$_2$Cl$_2$ (dehydrated, >99.5%), and K$_2$CO$_3$ (>99.5%) were purchased from Kanto Chemical Co. Inc. 5,5-dibromo-2,2′-bipyridine (>98.0%), 9-phenyl-2,7-bis(4,4,5,5-tetramethyl-1,3,2-dioxaborolan-2-yl)-9H-carbazole (>96.0%), 1,4-phenylenediboronic acid, 9-phenyl-carbazole (>98.0%), 2,1,3-benzothiadiazole (>99.0%) were purchased from Tokyo Chemical Industry Co., Ltd. Tetrakis(triphenylphosphine)palladium (Pd(PPh$_3$)$_4$; >90.0%), triethanolamine (TEOA; >98.0%), p-toluenesulfonic acid (>99.0%), ethylenediamine tetraacetic acid (>99.0%), and Bis-Tris (>99.0%) were purchased from Wako Pure Chemical Industries. These materials were used without any further purification. [Ru(CO)$_2$Cl$_2$]$_n$ was prepared according to a literature procedure.[50]

Synthesis

Ru(5,5-dibromo-2,2′-bipyridine)(CO)$_2$Cl$_2$. A MeOH solution (5 mL) containing [Ru(CO)$_2$Cl$_2$]$_n$ (103 mg, 0.45 mmol) and 5,5-dibromo-2,2′-bipyridine (145 mg, 0.46 mmol) was stirred under reflux for 1 h under N$_2$ atmosphere. After refluxing, the obtained precipitate was filtered and washed with CHCl$_3$ (25 mL) for three times giving a pale-yellow powder. Yield 113 mg (0.21 mmol, 46%). ^{1}H NMR (400 MHz, DMSO-d_6): δ = 9.35 (d, J = 1.6 Hz), 8.79 (d, J = 8.8 Hz), 8.72 (dd, J = 8.8, 1.6 Hz). FT-IR (MeOH): ν_{CO} = 2069, 2009 cm^{-1}.

[Cz-bpy]$_n$. A DMF–H$_2$O (5 : 1, v/v; 12 mL) solution containing 5,5′-dibromo-2,2′-bipyridine (314.8 mg, 1.0 mmol), 9-phenyl-2,7-bis(4,4,5,5-tetramethyl-1,3,2-dioxaborolan-2-yl)-9H-carbazole (497.9 mg, 1.0 mmol), K$_2$CO$_3$ (1040 mg, 7.5 mmol), and Pd(PPh$_3$)$_4$ (23.5 mg, 0.02 mmol) was stirred under reflux for 2 days under N$_2$ atmosphere. The obtained precipitate was filtered and washed with water (20 mL), MeOH (20 mL), and CH$_2$Cl$_2$ (20 mL). Yield 256 mg.

The same protocol was applied for the syntheses of **[Ph-bpy]$_n$** and **[Bt-bpy]$_n$** by using 1,4-phenylenediboronic acid and 4,7-bis(4,4,5,5-tetramethyl-1,3,2-dioxaborolan-2-yl)-2,1,3-benzothiadiazole, respectively, as the starting material instead of 9-phenyl-2,7-bis(4,4,5,5-tetramethyl-1,3,2-dioxaborolan-2-yl)-9H-carbazole. Their characterization data are shown in Fig. S1–S4.†

[Cz-bpyRu]$_n$. This compound was synthesized via two routes.

Route A. A MeOH dispersion (5 mL) containing [Ru(CO)$_2$Cl$_2$]$_n$ (22.8 mg, 0.10 mmol) and **[Cz-bpy]$_n$** (42.9 mg, 0.10 mmol) was refluxed with stirring for 17 h under the N$_2$ atmosphere. After refluxing, the obtained precipitate was filtered and washed with MeOH (20 mL). Yield 62.9 mg. FT-IR (ATR): ν_{CO} = 2054, 1990 cm^{-1}. Elemental analysis calcd. for C$_{30}$H$_{19}$Cl$_2$N$_3$O$_2$Ru (**Cz-bpyRu**): C, 57.61; H, 3.06; N, 6.72. Found: C, 57.50; H, 3.20; N, 6.81.

Route B. A DMF–H$_2$O (5 : 1, v/v; 12 mL) solution containing Ru(5,5-dibromo-2,2′-bipyridine)(CO)$_2$Cl$_2$ (27.0 mg, 0.05 mmol), 9-phenyl-2,7-bis(4,4,5,5-tetramethyl-1,3,2-dioxaborolan-2-yl)-9H-carbazole (24.8 mg, 0.05 mmol), K$_2$CO$_3$ (55.2 mg, 0.40 mmol), and Pd(PPh$_3$)$_4$ (1.0 mg, 1 μmol) was stirred at reflux for 2 days under a N$_2$ atmosphere. The obtained precipitate was filtered and washed with water (20 mL) and MeOH (20 mL). Yield 14.4 mg. FT-IR (ATR): ν_{CO} = 2019, 1923 cm^{-1}.

The protocol same as used in Route A was applied for the syntheses of **[Ph-bpyRu]$_n$** and **[Bt-bpyRu]$_n$** by using **[Ph-bpy]$_n$** and **[Bt-bpy]$_n$**, respectively, as starting materials instead of **[Cz-bpy]$_n$**. Elemental analysis calcd. for C$_{52}$H$_{36}$Cl$_4$N$_6$O$_4$Ru$_3$ (**[Ph-bpyRu]$_2$[Ph-bpy]$_1$**): C, 54.18; H, 3.15; N, 7.29. Found: C, 55.16; H, 3.15; N, 7.47. Elemental analysis calcd. for C$_{88}$H$_{50}$Cl$_8$N$_{10}$O$_8$Ru$_4$S$_5$ (**[Bt-bpyRu]$_4$[Bt-bpy]$_1$**): C, 44.72; H, 2.13; N, 11.85. Found: C, 44.52; H, 2.31; N, 11.82. Further characterization data are shown in Fig. S1–S7.†

Time-resolved microwave conductivity measurement

Time-resolved microwave conductivity experiments were performed using a third harmonic generator (THG; 355 nm) of an Nd:YAG laser (Continuum Inc., Surelite II, 5–8 ns pulse duration, 10 Hz) as the excitation source (9.1 × 10^{15} photons per cm^2 per pulse) and X-band microwave (~9.1 GHz) as the probe. The photoconductivity $\Delta\sigma$ was obtained using eqn (1)

$$\Delta\sigma = \Delta P_r/(AP_r) \tag{1}$$

where ΔP_r, A, and P_r are the transient power change of the reflected microwave power, the sensitivity factor, and the reflected microwave power, respectively. The transient photoconductivity $\Delta\sigma$ was converted to the product of the quantum yield (ϕ) and the sum of charge carrier mobilities $\Sigma\mu$ using eqn (2) and (3)

$$\Sigma\mu = \mu_+ + \mu_- \tag{2}$$

$$\phi\Sigma\mu = \Delta\sigma/(eI_0 F_{light}) \tag{3}$$

where e and F_{light} are the unit charge of a single electron and a correction (or filling) factor, respectively. The experiments were performed in air at room temperature (298 K).

Time-resolved infrared absorption spectroscopy

The time-resolved infrared absorption measurements were performed using the spectrometer described previously.[51] The powder sample was mixed with KCl powder, pelletized, and set in an IR cell filled with 20 torr N$_2$. The measurements were performed using the pump-probe method with a Ti: sapphire regenerative amplifier (Spectra Physics, Solstice. 90 fs duration,

1 kHz repetition rate) and optical parametric amplifiers (OPAs; Spectra Physics, TOPAS Prime). The sample was photoexcited by a 420 nm pulse (0.5 μJ per pulse, 500 Hz) from the OPA. The probe MIR pulse was generated by the difference frequency generation between the signal and idler from the OPA in an AgGaS$_2$ crystal and was detected with a 128-channel linear MCT array detector (Infrared Systems Development, FPAS-0144). The MIR signal was analysed after subtraction of smooth backgrounds from the spectra.

Photocatalytic reactions

A MeCN-TEOA dispersion (2 mL) of **[X-bpyM]$_n$** (X = Cz, Ph, or Bt; M = none or Ru) was placed in a Pyrex test tube (inner diameter: 10 mm; volume: 8.4 mL), degassed with CO_2 or N_2 bubbling (20 min), and sealed using a rubber septum prior to the photoirradiation. The sample tube was placed in a LED merry-go-round apparatus (Iris-MG-S, Cell System Inc.) and irradiated with visible light ($\lambda > 400$ nm) under stirring. The gaseous products, *i.e.*, CO and H$_2$ were analyzed using a Shimadzu GC-2010 gas chromatograph (MS-5A column, Ar carrier) combined with a TCD detector. The formate produced in the liquid phase was analyzed using a Shimadzu LC-20AT HPLC system equipped with two Shimadzu Shim-pack FAST-OA columns (100 × 7.8 mm) and a Shimadzu CDD-10A conductivity detector. An aqueous solution containing *p*-toluene-sulfonic acid (0.95 g L^{-1}) was used as the eluent at a flow rate of 0.8 mL min^{-1} (column temperature: 313 K). After column separation, the eluent was mixed with an aqueous solution containing *p*-toluenesulfonic acid (0.95 g L^{-1}), and ethyl-enediaminetetraacetic acid (0.03 g L^{-1}), and Bis-Tris (4.18 g L^{-1}). For wavelength dependency measurements, a LED lamp with an independent wavelength centered at 430, 450, 470, 505, or 525 nm (CL-H1 series, Asahi Spectra Co.) was used at a fixed photon flux of 2.1×10^{-7} einstein per s, instead of the afore-mentioned LED merry-go-round system. The external quantum efficiencies of photocatalytic formate formation (EQE$_{formate}$) were determined on the basis of eqn (4):

$$\text{EQE}_{formate} = \frac{n \times \text{amount of formate produced (mol)}}{\text{inputted photon (einstein)}} \quad (4)$$

where n indicates the number of electrons required to generate one molecule of the product (*i.e.*, 2 for formate formation by CO_2 reduction).

Computational details

Geometry optimizations were performed using the density functional theory (DFT) with ωB97X-D exchange-correlation functional.[52] For core electrons of Ru ([Ar]3d^{10}), Stuttgart/Dresden pseudopotentials[53] at the multi Dirac–Fock level were used. Corresponding double-ζ basis sets were adopted to valence orbitals of Ru. For other elements, namely, C, H, Cl, N, O and S, correlation-consistent basis sets at double-ζ level termed cc-pVDZ[54,55] were employed. Harmonic vibrational frequencies were also calculated analytically to confirm whether the optimized structure converged to an equilibrium geometry point. For the optimized structure, single-point calculations were performed using time-dependent DFT with the ωB97X-D functional to obtain the electronic structure in the T$_1$ state. Mulliken atomic charges in the S$_0$ and T$_1$ states were evaluated at the S$_0$ optimized structure. All calculations were performed by Gaussian 09 program.[56]

Conflicts of interest

There are no conflicts to declare.

Acknowledgements

Notes and references

1 C. A. Trickett, A. Helal, B. A. Al-Maythalony, Z. H. Yamani, K. E. Cordova and O. M. Yaghi, *Nat. Rev. Mater.*, 2017, **2**, 17045.

2 Y. Zheng, W. Zhang, Y. Li, J. Chen, B. Yu, J. Wang, L. Zhang and J. Zhang, *Nano Energy*, 2017, **40**, 512–539.

3 A. M. Appel, J. E. Bercaw, A. B. Bocarsly, H. Dobbek, D. L. DuBois, M. Dupuis, J. G. Ferry, E. Fujita, R. Hille, P. J. Kenis, C. A. Kerfeld, R. H. Morris, C. H. Peden, A. R. Portis, S. W. Ragsdale, T. B. Rauchfuss, J. N. Reek, L. C. Seefeldt, R. K. Thauer and G. L. Waldrop, *Chem. Rev.*, 2013, **113**, 6621–6658.

4 J. Artz, T. E. Müller, K. Thenert, J. Kleinekorte, R. Meys, A. Sternberg, A. Bardow and W. Leitner, *Chem. Rev.*, 2018, **118**, 434–504.

5 D. T. Whipple and P. J. A. Kenis, *J. Phys. Chem. Lett.*, 2010, **1**, 3451–3458.

6 C. Costentin, M. Robert and J. M. Saveant, *Chem. Soc. Rev.*, 2013, **42**, 2423–2436.

7 S. C. Roy, O. K. Varghese, M. Paulose and C. A. Grimes, *ACS Nano*, 2010, **4**, 1259–1278.

8 J. L. White, M. F. Baruch, J. E. Pander, Y. Hu, I. C. Fortmeyer, J. E. Park, T. Zhang, K. Liao, J. Gu, Y. Yan, T. W. Shaw, E. Abelev and A. B. Bocarsly, *Chem. Rev.*, 2015, **115**, 12888–12935.

9 C. Song, *Catal. Today*, 2006, **115**, 2–32.

10 G. Centi and S. Perathoner, *Catal. Today*, 2009, **148**, 191–205.

11 O. S. Bushuyev, P. De Luna, C. T. Dinh, L. Tao, G. Saur, J. van de Lagemaat, S. O. Kelley and E. H. Sargent, *Joule*, 2018, **2**, 825–832.

12 A. J. Morris, G. J. Meyer and E. Fujita, *Acc. Chem. Res.*, 2009, **42**, 1983–1994.

13 Y. Yamazaki, H. Takeda and O. Ishitani, *J. Photochem. Photobiol., C*, 2015, **25**, 106–137.

14 S. N. Habisreutinger, L. Schmidt-Mende and J. K. Stolarczyk, *Angew. Chem., Int. Ed.*, 2013, **52**, 7372–7408.

This journal is © The Royal Society of Chemistry 2022

J. Mater. Chem. A, 2022, **10**, 19821–19828 | **19827**

15 Y. Ma, X. Wang, Y. Jia, X. Chen, H. Han and C. Li, *Chem. Rev.*, 2014, **114**, 9987–10043.

16 S. Yoshino, T. Takayama, Y. Yamaguchi, A. Iwase and A. Kudo, *Acc. Chem. Res.*, 2022, **55**, 966–977.

17 H. Kageyama, K. Hayashi, K. Maeda, J. P. Attfield, Z. Hiroi, J. M. Rondinelli and K. R. Poeppelmeier, *Nat. Commun.*, 2018, **9**, 772.

18 H. Takeda, C. Cometto, O. Ishitani and M. Robert, *ACS Catal.*, 2016, **7**, 70–88.

19 Q. Wang and K. Domen, *Chem. Rev.*, 2020, **120**, 919–985.

20 K. Maeda, *Phys. Chem. Chem. Phys.*, 2013, **15**, 10537–10548.

21 Y. Wang, H. Suzuki, J. Xie, O. Tomita, D. J. Martin, M. Higashi, D. Kong, R. Abe and J. Tang, *Chem. Rev.*, 2018, **118**, 5201–5241.

22 F. E. Osterloh, *Chem. Soc. Rev.*, 2013, **42**, 2294–2320.

23 Y. H. Hong, Y. M. Lee, W. Nam and S. Fukuzumi, *J. Am. Chem. Soc.*, 2022, **144**, 695–700.

24 K. E. Dalle, J. Warnan, J. J. Leung, B. Reuillard, S. Isabell and E. Reisner, *Chem. Rev.*, 2019, **119**, 2752–2875.

25 T. Morikawa, S. Sato, K. Sekizawa, T. M. Suzuki and T. Arai, *Acc. Chem. Res.*, 2022, **55**, 933–943.

26 A. Nakada, H. Kumagai, M. Robert, O. Ishitani and K. Maeda, *Acc. Mater. Res.*, 2021, **2**, 458–470.

27 C. Dai and B. Liu, *Energy Environ. Sci.*, 2020, **13**, 24–52.

28 J. M. Lee and A. I. Cooper, *Chem. Rev.*, 2020, **120**, 2171–2214.

29 Y. Wang, A. Vogel, M. Sachs, R. S. Sprick, L. Wilbraham, S. J. A. Moniz, R. Godin, M. A. Zwijnenburg, J. R. Durrant, A. I. Cooper and J. Tang, *Nat. Energy*, 2019, **4**, 746–760.

30 C. Yang, W. Huang, L. C. da Silva, K. A. I. Zhang and X. Wang, *Chem.–Eur. J.*, 2018, **24**, 17454–17458.

31 H.-P. Liang, A. Acharjya, D. A. Anito, S. Vogl, T.-X. Wang, A. Thomas and B.-H. Han, *ACS Catal.*, 2019, **9**, 3959–3968.

32 X. Yu, Z. Yang, B. Qiu, S. Guo, P. Yang, B. Yu, H. Zhang, Y. Zhao, X. Yang, B. Han and Z. Liu, *Angew. Chem., Int. Ed.*, 2019, **58**, 632–636.

33 Z. Fu, X. Wang, A. M. Gardner, X. Wang, S. Y. Chong, G. Neri, A. J. Cowan, L. Liu, X. Li, A. Vogel, R. Clowes, M. Bilton, L. Chen, R. S. Sprick and A. I. Cooper, *Chem. Sci.*, 2020, **11**, 543–550.

34 X. Y. Dong, Y. N. Si, Q. Y. Wang, S. Wang and S. Q. Zang, *Adv. Mater.*, 2021, **33**, 2101568.

35 J. Li, K. Ma, Y. He, S. Ren, C. Li, X.-B. Chen, Z. Shi and S. Feng, *Catal.: Sci. Technol.*, 2021, **11**, 7300–7306.

36 G. E. M. Schukraft, R. T. Woodward, S. Kumar, M. Sachs, S. Eslava and C. Petit, *ChemSusChem*, 2021, **14**, 1720–1727.

37 L. Hou, G. Tang, H. Huang, S. Yin, B. Long, A. Ali, G.-J. Deng and T. Song, *J. Mater. Chem. A*, 2022, **10**, 5287–5294.

38 S. Barman, A. Singh, F. A. Rahimi and T. K. Maji, *J. Am. Chem. Soc.*, 2021, **143**, 16284–16292.

39 R. Kuriki and K. Maeda, *Phys. Chem. Chem. Phys.*, 2017, **19**, 4938–4950.

40 G. Gerbaud, J. M. Mouesca, S. Hediger, S. Chardon-Noblat, F. Lafolet, A. Deronzier and M. Bardet, *Phys. Chem. Chem. Phys.*, 2010, **12**, 15428–15435.

41 Y. Tamaki, T. Morimoto, K. Koike and O. Ishitani, *Proc. Natl. Acad. Sci. U. S. A.*, 2012, **109**, 15673–15678.

42 Y. Nakayama, S. Machida, D. Tsunami, Y. Kimura, M. Niwano, Y. Noguchi and H. Ishii, *Appl. Phys. Lett.*, 2008, **92**, 153306.

43 A. A. Vlček, *Coord. Chem. Rev.*, 1982, **43**, 39–62.

44 A. Saeki, S. Yoshikawa, M. Tsuji, Y. Koizumi, M. Ide, C. Vijayakumar and S. Seki, *J. Am. Chem. Soc.*, 2012, **134**, 19035–19042.

45 C. W. Machan, M. D. Sampson and C. P. Kubiak, *J. Am. Chem. Soc.*, 2015, **137**, 8564–8571.

46 A. Yamakata, T.-a. Ishibashi and H. Onishi, *Bull. Chem. Soc. Jpn.*, 2002, **75**, 1019–1022.

47 K. Shibata, K. Kato, C. Tsounis, T. Kanazawa, D. Lu, S. Nozawa, A. Yamakata, O. Ishitani and K. Maeda, *Sol. RRL*, 2019, **4**, 1900461.

48 C. Tsounis, R. Kuriki, K. Shibata, J. J. M. Vequizo, D. Lu, A. Yamakata, O. Ishitani, R. Amal and K. Maeda, *ACS Sustainable Chem. Eng.*, 2018, **6**, 15333–15340.

49 A. Nakada, M. Higashi, T. Kimura, H. Suzuki, D. Kato, H. Okajima, T. Yamamoto, A. Saeki, H. Kageyama and R. Abe, *Chem. Mater.*, 2019, **31**, 3419–3429.

50 P. A. Anderson, G. B. Deacon, K. H. Haarmann, F. R. Keene, T. J. Meyer, D. A. Reitsma, B. W. Skelton, G. F. Strouse, N. C. Thomas, J. A. Treadway and A. H. White, *Inorg. Chem.*, 1995, **34**, 6145–6157.

51 A. Yamakata, M. Kawaguchi, N. Nishimura, T. Minegishi, J. Kubota and K. Domen, *J. Phys. Chem. C*, 2014, **118**, 23897–23906.

52 J.-D. Chai and M. Head-Gordon, *Phys. Chem. Chem. Phys.*, 2008, **10**, 6615–6620.

53 K. A. Peterson, D. Figgen, M. Dolg and H. Stoll, *J. Chem. Phys.*, 2007, **126**, 124101–124112.

54 T. H. Dunning, *J. Chem. Phys.*, 1989, **90**, 1007–1023.

55 D. E. Woon and T. H. Dunning, *J. Chem. Phys.*, 1993, **98**, 1358–1371.

56 M. J. Frisch, G. W. Trucks, H. B. Schlegel, G. E. Scuseria, M. A. Robb, J. R. Cheeseman, G. Scalmani, V. Barone, B. Mennucci, G. A. Petersson, H. Nakatsuji, M. Caricato, X. Li, H. P. Hratchian, A. F. Izmaylov, J. Bloino, G. Zheng, J. L. Sonnenberg, M. Hada, M. Ehara, K. Toyota, R. Fukuda, J. Hasegawa, M. Ishida, T. Nakajima, Y. Honda, O. Kitao, H. Nakai, T. Vreven, J. A. Montgomery Jr, J. E. Peralta, F. Ogliaro, M. Bearpark, J. J. Heyd, E. Brothers, K. N. Kudin, V. N. Staroverov, T. Keith, R. Kobayashi, J. Normand, K. Raghavachari, M. Klene, J. E. Knox, J. B. Cross, V. Bakken, C. Adamo, J. Jaramillo, R. Gomperts, R. E. Stratmann, O. Yazyev, A. J. Austin, R. Cammi, C. Pomelli, J. W. Ochterski, R. L. Martin, K. Morokuma, V. G. Zakrzewski, G. A. Voth, P. Salvador, J. J. Dannenberg, S. Dapprich, A. D. Daniels, O. Farkas, J. B. Foresman, J. V. Ortiz, J. Cioslowski and D. J. Fox, *Gaussian 09, Rev. C.01*, Gaussian, Inc., Wallingford, CT, 2010.